Predictions for particle deposition from LES of ribbed channel flow

G. Lo Iacono [a],*, P.G. Tucker [b], A.M. Reynolds [a]

[a] *Biomathematics and Bioinformatics Division, Rothamsted Research, Harpenden, Hertfordshire AL5 2JQ, UK*
[b] *Civil and Computational Engineering Centre, University of Wales, Swansea, UK*

Abstract

Predictions for the deposition of spherical and cylindrical particles from a ribbed channel flow onto adjacent flow boundaries are obtained using *large eddy simulation* (*LES*) under the assumption of one-way coupling. Results indicate that spherical particles tend to accumulate on the vertical rib wall facing the mean-flow direction with little particle deposition onto surfaces immediately downstream of the rib. This preferential deposition is not predicted for cylindrical particles.
© 2005 Elsevier Inc. All rights reserved.

Keywords: LES; Particle deposition; Fibres; Ribbed channel

1. Introduction

Particle deposition from ribbed channel flows is of considerable practical importance. It is, for example, responsible for defects in microelectronics devices during fabrication and subsequent causes of failure during operation, microbiological contamination of food products during processing and the fouling of heat exchangers.

Unsteady Reynolds averaged Navier–Stokes (URANS) based electronic system particle transport studies are given in Tucker (2001a). However, poor agreement is found with measurements. Much of this is attributed to the URANS modelling which gives rise to poor turbulence statistic predictions (see Tucker and Pan, 2001). More importantly, RANS models only predict the mean-flow and the turbulent kinetic energy and not the instantaneous flow which advects particles. Consequently the RANS model must be supplemented by an additional model for the fluid–velocity fluctuations

experienced by particles along their trajectories. For the case considered by Tucker (2001a), the use of LES significantly improves turbulence statistics (Chung and Tucker, 2003) and avoids the need to stochastically model fluid–velocity fluctuations. Hence the LES approach is further considered here. The particle deposition predictions of Tucker (2001a) assume spherical particles. To address the significance of particle shape in determining particle deposition, the results of a preliminary study of cylindrical particle movements are also presented. The model of cylindrical particles is intended to be straightforward to implement in general CFD solvers and applicable to a relatively wide range of the Reynolds numbers Re_d (based on the diameter of the cylinder) and Re_l (based on the length of the cylinder). Previous methods do not entirely satisfy these demands. For example the equations of Olson and Kerekes (1998) are only valid for inertial-less particles. Fan and Ahmadi (1990, 1995a,b) and Zhang et al. (2001) use the ellipsoidal particle drag/torque expressions of Jeffery (1922). Unfortunately these and the adopted formalism (based on Euler angles), although rigorous, are not simple to implement. For example, the torque is a function of the spatial derivative of the flow velocity, in the particle

---

* Corresponding author. Tel.: +44 1582 763 133; fax: +44 1582 760 981.
E-mail address: giovanni.loiacono@bbsrc.ac.uk (G. Lo Iacono).

frame of reference. In addition, these models are valid only for the creeping flows. Here, a new, relatively easy to implement cylindrical particle model is presented.

2. Governing equations and their numerical solution

2.1. Flow field equations

In LES, the flow variables are decomposed into resolved scales, associated with the larger eddies, and the modelled sub-grid scales, related to the more universal smaller eddies. The resolved scales $\bar{u}$ are obtained through a filtering procedure:

$$\bar{u}(\mathbf{x}) = \int_D u(\mathbf{x}')G(\mathbf{x}, \mathbf{x}')d\mathbf{x}' \tag{1}$$

where D is the computational domain, G the filter function, and $\mathbf{x}$ and $\mathbf{x}'$ represent the vector position. The continuity and Navier–Stokes equations are rewritten according to the previous decomposition and then filtered. This procedure leads to the following governing equations for LES:

$$\frac{\partial \bar{u}_\alpha}{\partial x_\alpha} = 0 \tag{2a}$$

$$\frac{\partial \bar{u}_\alpha}{\partial t} + \frac{\partial}{\partial x_\beta}(\bar{u}_\alpha \bar{u}_\beta) = -\frac{1}{\rho}\frac{\partial \bar{p}}{\partial x_\alpha} - \frac{\partial \tau_{\alpha\beta}}{\partial x_\beta} + v\frac{\partial}{\partial x_\beta}\left(\frac{\partial \bar{u}_\alpha}{\partial x_\beta} + \frac{\partial \bar{u}_\beta}{\partial x_\alpha}\right) \tag{2b}$$

where ρ is the fluid density, $\tau_{\alpha\beta} = \overline{u_\alpha u_\beta} - \bar{u}_\alpha \bar{u}_\beta$ is the SGS (sub-grid scale) stress, representing the interaction between small and larger scales. Thus the basic LES problem is to find an appropriate model for the SGS stresses represented by $\tau_{\alpha\beta}$. Smagorinsky (1963) postulated the form of SGS stresses as $\tau_{\alpha\beta} = 2v_T\bar{S}_{\alpha\beta}$ where the eddy viscosity $v_T = C\bar{\Delta}^2|\bar{S}|$ and $\bar{S}_{\alpha\beta} = (\partial \bar{u}_\alpha/\partial x_\beta + \partial \bar{u}_\beta/\partial x_\alpha)$ is the strain rate in the resolved velocity field. $\bar{\Delta}$ is a length scale associated with the filter width (or mesh size) and C is a constant (Smagorinsky's constant). Here $\bar{\Delta} = (\bar{\Delta}_x\bar{\Delta}_y\bar{\Delta}_z)^{1/3}$ where $\bar{\Delta}_{x(y,z)}$ is the filter width (or mesh size) in the x (y, z) direction. Nevertheless the real behaviour of eddies is more complicated than the model. Hence the value of C depends on the flow. Here, for homogeneous and isotropic turbulence $C = 0.2$ (as in Yeh and Lei, 1991), and $C = 0.1$ for all the other cases (see Deardoff, 1970; Meneveau, 1994).

2.2. Particulate phase equations

The particles are treated as individual, small, rigid bodies. The fluid phase is assumed not to be affected by them. The gravity, drag and (for wall-bounded flows) Saffman lift forces are considered. The effects of the unresolved sub-grid scales on particle motion are not considered here. These effects were studied by Wang and Squires (1996), who performed a simulation at two different Reynolds numbers (based on the on the friction velocity), $Re_\tau = 180$ and $Re_\tau = 1000$ in a vertical channel. Their results are in reasonable agreement with the direct numerical simulation (DNS) data of McLaughlin (1989) showing the capability of LES in predicting the behaviour of particles. Discrepancies between LES and DNS results became apparent when the timescale associated with the smallest revolved scales of motions is comparable to the particle relaxation time. Despite this, predictions for particle deposition were not found to depend sensitively upon the sub-grid scales. These findings are supported by those of Armenio et al. (1999a,b) who concluded that that filter operator in LES causes an underestimation of the settling velocity, but that other particle statistics (e.g. average position of particles, distribution after deposition) are predicted more accurately. Consequently, it can be anticipated that the motions of cylindrical particles studied here, which have particle relaxation times that are much large than the timescales associated with the near-wall turbulence, will not be sensitively dependent upon the sub-grid scales of motion.

2.2.1. Spherical particles

For a sphere, the particle relaxation time is defined as: $\tau_p = 4\rho_p d_p^2/(3\mu C_d Re_p)$, where ρ_p and d_p are respectively the density and diameter of the particle and μ is the fluid viscosity. Also, C_d is the drag coefficient, given by $C_d = 24/Re_p$ if $Re_p \leqslant 0.5$ and $C_d = 24(1 + 0.15Re_p^{0.687})/Re_p$ if $0.5 < Re_p < 10^3$ (see Clift et al., 1978). In the former expressions Re_p is the particle Reynolds number defined as: $Re_p = \rho d_p|\mathbf{u}_p - \mathbf{u}_f|/\mu$ where $\mathbf{u}_p$ and $\mathbf{u}_f$ are respectively the particle and local fluid. When the particle density is much greater than the fluid density, as in all the cases considered here, the particle momentum equation effectively reduces to Stokes drag, gravitational settlement and Saffman lift (Saffman, 1965):

$$m_p\frac{d\mathbf{u}_p}{dt} = \frac{1}{2}\rho_p C_d A|\mathbf{u}_p - \mathbf{u}_f|(u_p - u_f) + m_p\mathbf{g} + \mathbf{L}_S \tag{3}$$

where $A = \pi d_p^2/4$ is the projected area of the particle, m_p is the mass of the particle, $\mathbf{g}$ the earth's acceleration due to gravity, which is expressed as $\mathbf{g} = g\mathbf{i}(\mathbf{j}, \mathbf{k})$, where $g = 9.8 \text{ m/s}^2$ and $\mathbf{i}(\mathbf{j}, \mathbf{k})$ represents the unitary vector in the x (y, z)-direction. The neglected terms include the added mass and the Basset history-term. The Saffman lift $\mathbf{L}_S$ is given by:

$$\mathbf{L}_S = 1.6d_p^2(\rho\mu)^{1/2}\left(\frac{1}{|\boldsymbol{\omega}_f|}\right)^{1/2}(\mathbf{u}_p - \mathbf{u}_f) \times \boldsymbol{\omega}_f f \tag{4}$$

where $\boldsymbol{\omega}_f = \text{curl } \mathbf{u}_f$ is the fluid vorticity and f is the high Re_p correction function of Mei (1992) which extends the validity of Eq. (4), to the range $Re_p \leqslant 100$. In all the simulations presented here $Re_p \approx O(1)$. It should

be noted that Eq. (3) does not include wall effects. For instance, near-wall particles experience a directionally dependent modified C_d (see Brenner, 1964). The expressions used here, are only valid if the distance of the particle from the wall is large in comparison d_p. When this distance is small other factors are also involved. These include the possible presence of electrical charge effects. However, following the DNS studies of McLaughlin (1989) we ignore these complex near-wall influences which could have some effect on the ribbed channel results.

2.2.2. Cylindrical particles

Fig. 1 shows an idealized cylindrical particle. The particle coordinate system $\mathbf{x}' = [x', y', z']$, with origin O' at the mass centre, is also shown. The orientation of the cylindrical particle is determined by the angle $\boldsymbol{\theta} = [\theta_x, \theta_y, \theta_z]$. The subscripts x, y, z refer to the axis of rotation. Herein, the axis of symmetry of the cylinder, represented by the vector $\mathbf{b}$, is referred to as the principal axis. The diameter of the section of the cylinder d_p is assumed to be much smaller than its length l. The main aspects of the model are explained in Figs. 1 and 2. The fluid element surrounding the point P has an average relative velocity $\mathbf{u}_f - \mathbf{u}_p$. The flow exerts a force in the direction of $(\mathbf{u}_f - \mathbf{u}_p)$. Here, for simplicity this is assumed to be in the x–z the plane. The total force $\mathbf{F}$ acting on this portion of cylinder (near the point P) by the surrounding fluid is decomposed into components perpendicular, and parallel, to the principal axis of the cylinder, called respectively D and S. The normal component D, which is also parallel to the plane composed by the vectors $\mathbf{b}$ and $(\mathbf{u}_f - \mathbf{u}_p)$, is modelled according the classical drag expression for a cylinder of infinite length (see Schlichting and Gersten, 2000):

$$D = \tfrac{1}{2} C_d \rho (\mathbf{u}_f - \mathbf{u}_p)^2_\perp d_p |\mathbf{b}| \tag{5}$$

where $(\mathbf{u}_f - \mathbf{u}_p)_\perp$ is the component of the relative velocity perpendicular to $\mathbf{b}$. Here C_d is the drag coefficient for a cylinder as measured by Wieselsberger (see Schlichting and Gersten, 2000). The parallel component S, is mod-
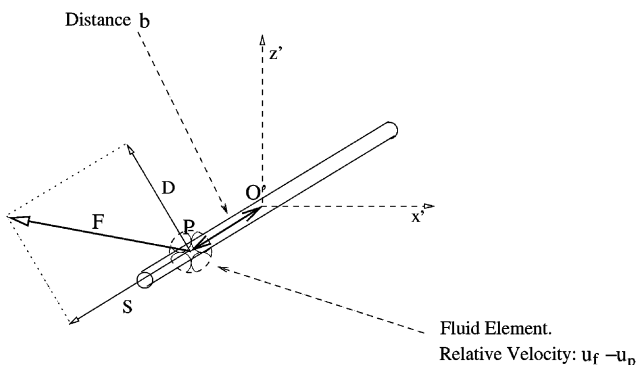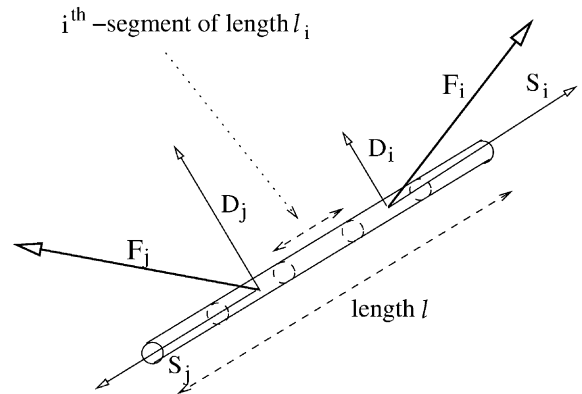
elled as the friction force acting on a flat plate of equivalent surface area to the cylinder, whose module per unitary surface is (see, for example Houghton and Carpenter, 1993):

$$S = \frac{2.6}{Re_l^{1/2}} \frac{1}{2} \rho (\mathbf{u}_f - \mathbf{u}_p)^2_\parallel \tag{6}$$

where $(\mathbf{u}_f - \mathbf{u}_p)_\parallel$ is the component of the relative velocity parallel to $\mathbf{b}$ and $Re_l = \rho l |\mathbf{u}_p - \mathbf{u}_f|/\mu$. Only the component normal to the principal axis, i.e. the D, generates a torque

$$\mathbf{T} = \mathbf{b} \times \mathbf{F} \text{ with module } |\mathbf{T}| = D|\mathbf{b}| \tag{7}$$

while S, being parallel to the axis, causes no rotation. At this stage, the fibre is decomposed in a series of i-segments. Each segment is treated as a cylinder of infinite length i.e. the end effects on drag are ignored. Then contributions D_i, S_i and $\mathbf{T}_i$, of all i elements along the fibre are calculated. This leads to the following resultant total forces $D = \sum_i D_i$, $S = \sum_i S_i$ and torque $\mathbf{T} = \sum_i \mathbf{T}_i$. The flow surrounding each segment is assumed uniform. Its velocity $\mathbf{u}_{fi}$ is obtained by interpolating the flow field at the centre of each segment. The total forces D and S cause translation of the cylinder. The torque $\mathbf{T}$ causes rotation around the mass centre. The equations of motion (translation and rotation) for a cylinder are therefore given by:

$$m_p \frac{du_\perp}{dt} = D, \quad m_p \frac{du_\parallel}{dt} = S, \quad I \frac{d\boldsymbol{\omega}_p}{dt} = \mathbf{T} \tag{8a}$$

and

$$u_\perp = \frac{dr_\perp}{dt}, \quad u_\parallel = \frac{dr_\parallel}{dt}, \quad \boldsymbol{\omega}_p = \frac{d\boldsymbol{\theta}_p}{dt} \tag{8b}$$

where $u_\perp$, $u_\parallel$, $r_\perp$, $r_\parallel$ are the translational velocities and displacements, respectively perpendicular and parallel to $\mathbf{b}$. I is the moment of inertia. While $\boldsymbol{\omega}_p$ and $\boldsymbol{\theta}_p$ are the angular velocity and displacement in the direction normal to the plane determined by $\mathbf{F}$ and $\mathbf{b}$.

In order to validate basic elements of the cylindrical particle model, comparisons with the analytical results

Fig. 2. i-Forces on each segment.

Fig. 1. Forces acting on a cylindrical particle.

of Khayat and Cox (1989) are made. According to the authors, at small $Re_d = \rho d_{\mathrm{p}}|\mathbf{u}_{\mathrm{p}} - \mathbf{u}_{\mathrm{f}}|/\mu$, the force $\mathbf{f}$ per unit length for an infinitely long cylinder in a uniform flow is:

$$\frac{\mathbf{f}}{2\pi\mu(|\mathbf{u}_{\mathrm{f}} - \mathbf{u}_{\mathrm{p}}|)} = \frac{1}{\ln Re_d}\left(\cos\theta\frac{\mathbf{b}}{|\mathbf{b}|} - 2\mathbf{e}\right)$$
$$- \left(\frac{1}{\ln Re_d}\right)^2\left\{\frac{1}{2}\left(\cos\theta\frac{\mathbf{b}}{|\mathbf{b}|} - 2\mathbf{e}\right)[\ln\sin\vartheta^2\right.$$
$$\left.+2(\gamma - \ln 4)] - \cos\theta\frac{\mathbf{b}}{|\mathbf{b}|} + \mathbf{e}\right\} \qquad (9)$$

where $\mathbf{e}$ is the direction of the relative velocity and γ is Euler's constant. It is clear that the force in (9) is composed of components parallel to the fibre $f_{\mathbf{d}}$, and parallel to the flow $f_{\mathbf{e}}$. In order to validate this model, the dependence of the forces $D(\theta)$ and $S(\theta)$ on θ (calculated by Eqs. (5) and (6)) is compared with the analytical expression given by (9). The $Re_d = 0.5$ results can be seen in Figs. 3 and 4 which give the dependence of the force acting on cylinder against the angle ϑ between the cylinder
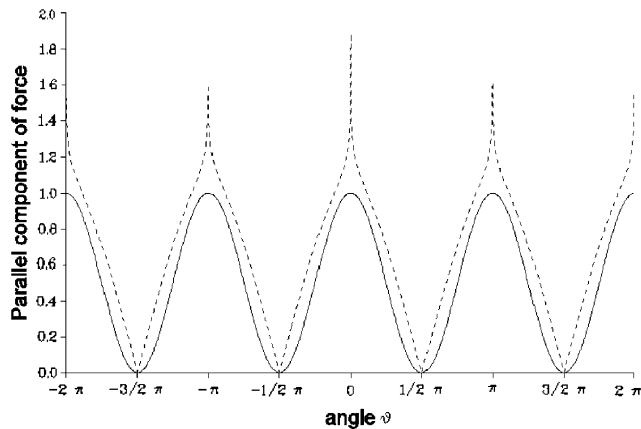

Fig. 3. Dependence of the parallel force component vs ϑ. (---) Cox and Khayat's model; (—) present model. Note, unlike the current model, the analytical model is not valid for $\sin\vartheta \approx 0$.
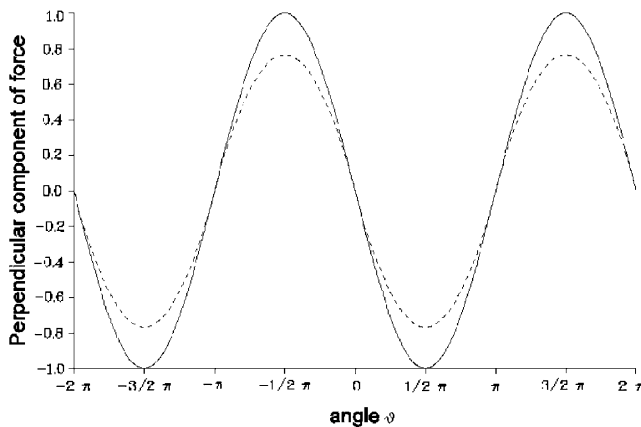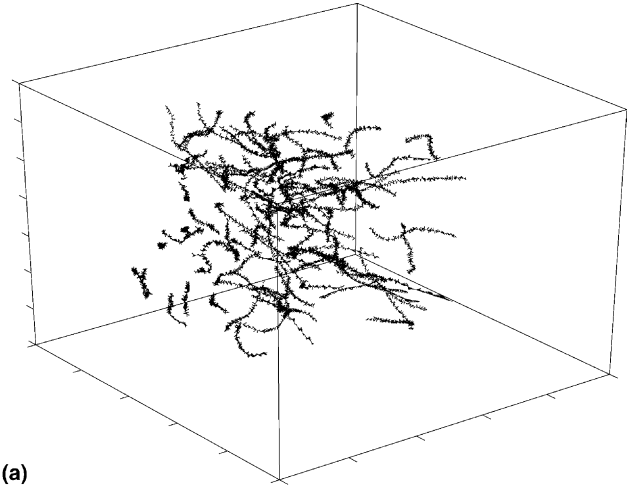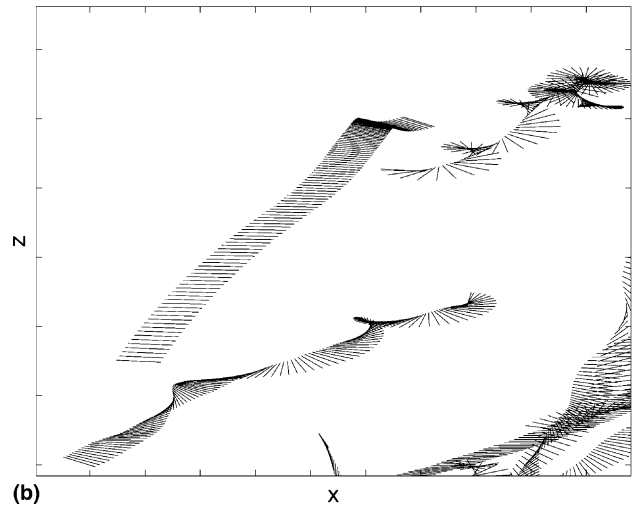

Fig. 4. Dependence of the perpendicular force component vs ϑ. (---) Cox and Khayat's model; (—) present model.

Fig. 5. (a) Motion of fibres in a turbulent flow at consecutive moments. (b) Zoomed in two-dimensional view of fibres in a turbulent flow at consecutive moments.

and flow. Figs. 3 and 4 give the parallel and normal force components, respectively. It is worthwhile noting that, unlike the current model, the model of Cox and Khayat ceases to be valid in the limit $\theta \to 0$, i.e. when the centreline is aligned with the flow direction. The comparison improves as $Re_d \to 0$. The model also predicts the existence of a terminal velocity in the presence of gravity. The linear and angular particle dispersions have the same behaviour predicted by the theory. Figs. 5a and b give the motions of fibres in homogeneous, isotropic turbulence. Fig. 5a is a global three-dimensional view and Fig. 5b a zoomed in two-dimensional view. As can be seen the fibres exhibit complex rotational and translational motions.

2.3. Numerical methods

The LES code of Tucker (2001b) is used. It has a range of LES models (see Tucker, 2004). However, since
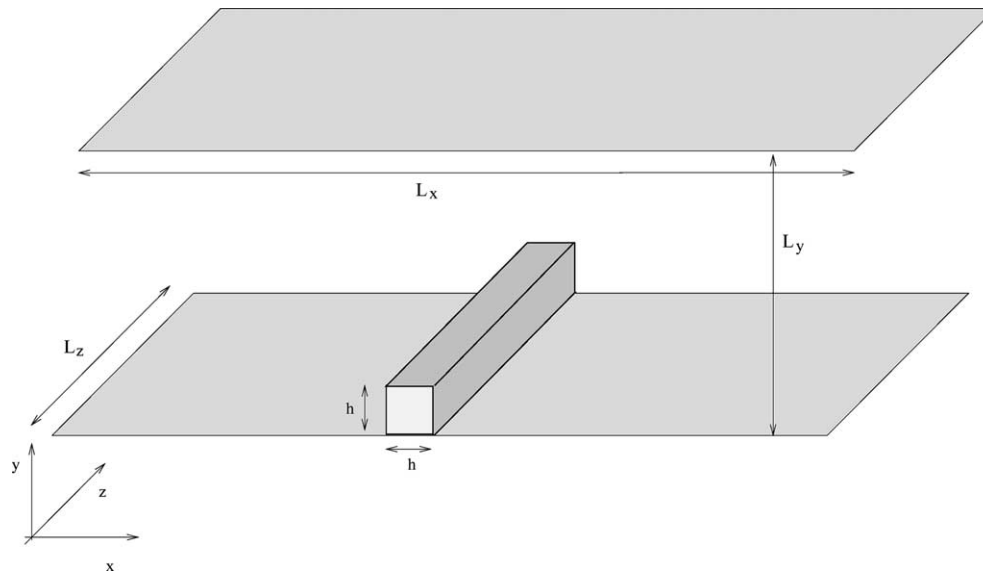
Fig. 6. Geometry and notation for the ribbed channel.

we are here mainly seeking qualitative ribbed channel flow deposition trends the Smagorinsky model is used. The governing equations are discretized in a centred, second-order, staggered grid, finite-difference framework. The Crank–Nicolson scheme is used to integrate the flow equations in time. At solid walls the usual no-slip and impermeability conditions are applied. For all the cases here, unless otherwise stated, at non-solid walls periodic boundary conditions are applied. Non-uniform grids use geometrical expansion (or contraction) with factor χ i.e. the mesh size Δ_i changes relatively to the adjacent mesh Δ_{i-1} as $\Delta_i = \chi \Delta_{i-1}$ (or $\Delta_i = \chi^{-1}\Delta_{i-1}$). Spherical and cylindrical particles are injected randomly in the computational domain with a velocity equal to the local fluid velocity. In order to calculate the trajectories of motion ((3) for spherical particles and (8a) and (8b) for cylindrical particles), a fourth-order Runge–Kutta method is adopted. The fibre is assumed to be composed by five segments. A sixth-order Lagrangian interpolation is used to evaluate the instantaneous velocity of the fluid at the particle locations for the spheres or at the centre of each segment for the cylindrical particles. The collision between particles and walls is assumed to be perfectly inelastic. i.e. when the particle surface reaches the wall, the particle velocity is set to 0.

3. Case details

The model and its numerical implementation were validated using experimental data for homogeneous and isotropic turbulence, plane channel flow and a mixing layer. More details can be found in Lo Iacono and Tucker (2003). Here, the ribbed channel case details are presented.

The channel geometry and some notations are given in Fig. 6. The mean flow is in the x direction. Comparison is made with the velocity measurements of Acharya et al. (1993). Simulations, on fine and coarse grids, are carried out. However, it has been observed that particle simulations on these show a similar behaviour. Therefore, to reduce computational costs and allow more studies, coarse grid results are also presented. The computational domain and other parameters of the simulation are given in Table 1.

Integration time steps are much less than the Kolmogorov dissipation timescale $t_\eta = T/Re^{1/2}$, where T is the timescale of which the largest eddies of size L_x evolve. The choice of these time steps also ensures that a fluid element does not travel for a distance longer than the mesh size. Grids vary smoothly with $\beta < 1.1$ everywhere. For the finer grid, in 'wall units' $2.5 < \Delta_x^+ < 20$, $0.5 < \Delta_y^+ < 20$ and $\Delta_z^+ \approx 8$. Here and throughout, the superscript, +, denotes quantities that have been rendered non-dimensional using the friction velocity u^*, calculated from the computed mean pressure gradient, and the kinematic viscosity v. Gravity mostly acts in

Table 1
Computational domain and simulation parameters for ribbed channel

Parameters	Value
Dimension of the square rib h	6.35 mm
Channel width L_y	10 h
Streamwise dimension L_x	20 h
Spanwise dimension L_z	10 h
$Re = u_0 L_y/2v$	7000
Number of grid points (coarse grid)	$113 \times 65 \times 33$
Number of grid points (fine grid)	$215 \times 215 \times 105$
Time step Δt (coarse grid)	1.0×10^{-4} s
Time step Δt (fine grid)	2.5×10^{-6} s

the z-direction. The number of particles is 8500. Simulations are stopped after a time equivalent to $6L_x/u_0$.

4. Ribbed channel results

Using velocity vectors, Fig. 7 shows the mid x–y plane instantaneous flow behaviour in the rib proximity. The grey scale contours give vorticity magnitudes. The streamwise distance x (measured from the centre of the rib) and the wall-normal distance y, are normalized by the rib height, h. Near the rib large scale vortex features typical of a separated flow can be observed. However, for $y/h > 2$ the flow appears almost laminar. Fig. 8 gives the isosurface of vorticity module. Coherent structures emanating from the rib leading edge can be observed while streaky structures can be noticed at the top smooth wall.

Fig. 9 plots the streamwise velocity near the rib, at $x/h = -0.5$, 0.0 and 0.6. These locations correspond to the left face, centre and close to the right face of the rib. Velocities are normalized by u_0. Here and throughout,

the continuous line represent the fine grid LES and the discontinuous line the coarse grid LES. As can be seen, the agreement with the measurements is encouraging. The recirculation downstream of the rib is reasonably
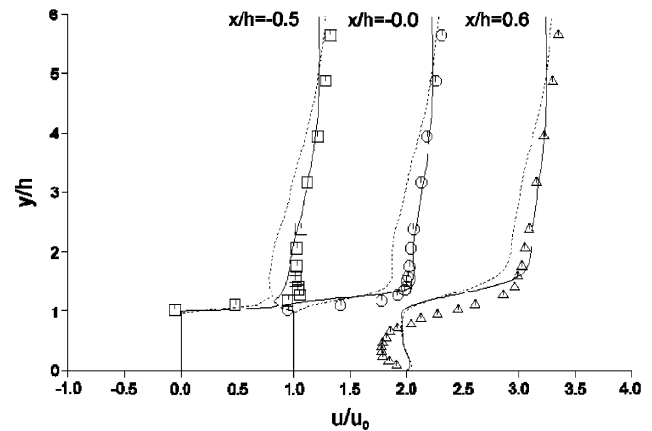

Fig. 9. Streamwise velocity distributions at $x/h = -0.5$, 0.0, 0.6. (- - -) Coarse grid; (—) fine grid.
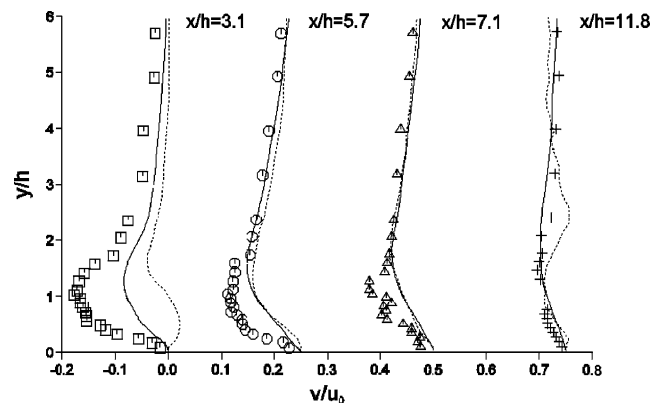

Fig. 10. Cross-stream velocity distributions at $x/h = 3.1$, 5.7, 7.1, 11.8. (- - -) Coarse grid; (—) fine grid.

Fig. 7. Vector velocity field in the proximity of the rib.

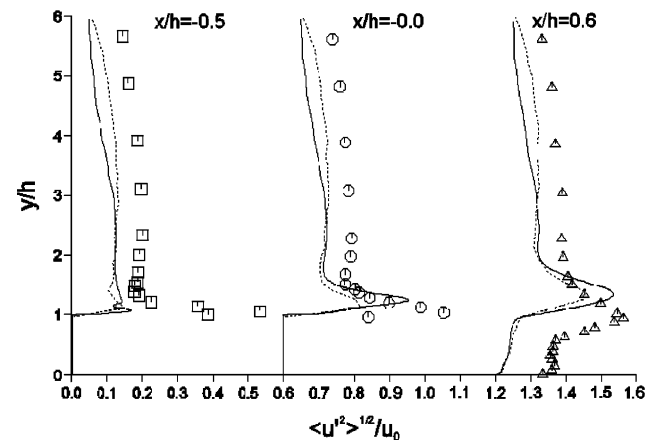Fig. 8. Isosurface of the vorticity module.

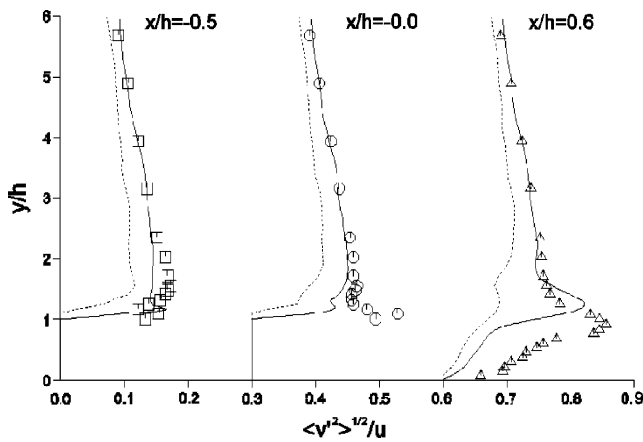Fig. 11. Streamwise velocity fluctuations at $x/h = -0.5$, 0.0, 0.6. (- - -) Coarse grid; (—) fine grid.

Fig. 12. Cross-stream velocity fluctuations at $x/h = -0.5, 0.0, 0.6$. (---) Coarse grid; (—) fine grid.
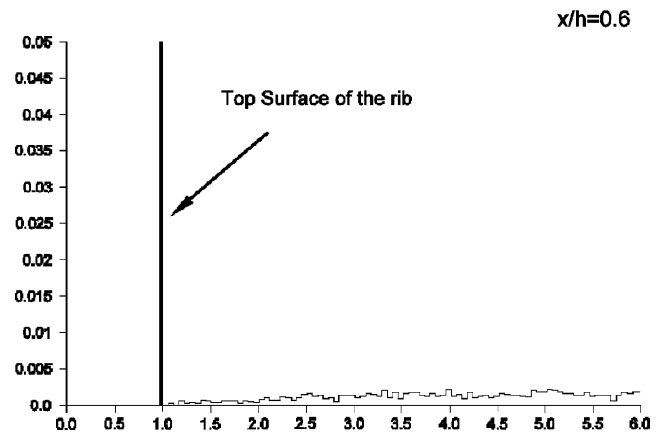

Fig. 14. Particle concentration at $x/h = 0.6$ for fine grid.
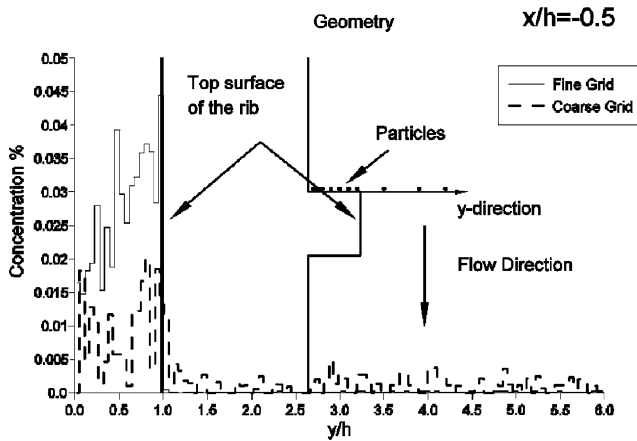

Fig. 13. Geometry and particle concentration at $x/h = -0.5$. (---) Coarse grid; (—) fine grid.

well captured. Streamwise velocities further downstream of the rib ($x/h = 3.1, 5.7, 7.11$ and 11.8) have a similar level of agreement with the measurements. However, as shown in Fig. 10, cross-stream velocities downstream of the rib especially for $x/h = 3.1$ tend to be over-predicted. Figs. 11 and 12 show the streamwise and cross-stream velocity fluctuations, near the rib, respectively. Peaks associated with shearing on top of the rib, and hence turbulence generation, are evident. The peak decreases in the streamwise direction. This behaviour is generally captured by the LES but the magnitudes are slightly under-predicted. As expected, a better agreement with measurements is obtained for the finer grid.

Vertical particle concentrations at the same x/h locations as considered for the flow, i.e. $x/h = -0.5, 0.0, 0.6, 3.1, \ldots$ have been computed. Figs. 13 and 14 show light particle ($d_p = 87\ \mu m$, $\rho_p = 1000\ kg/m^3$) concentration at $x/h = -0.5$ and 0.6 respectively. The gravity direction $\mathbf{g} = g\mathbf{k}$. Fig. 13 also shows data for the coarse
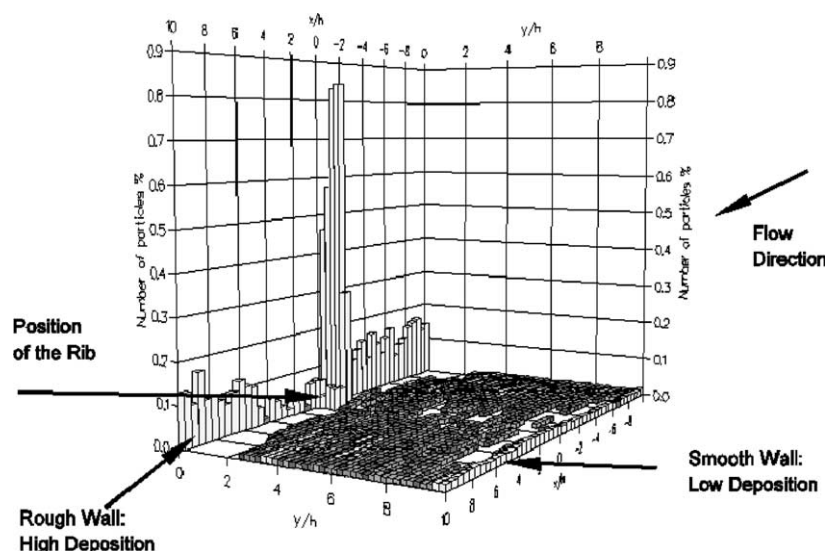

Fig. 15. Particle concentration.

grid (discontinuous line). In order to make the figures clearer, data are visualized only for $y/h < 6$ (roughly the bottom half of the channel); in addition the high depositions onto the bottom wall (i.e. at $y/h = 0$) are not displayed here. The figures imply, in general agreement with the observations of Chamberlain et al. (1984), that spherical particles accumulate on the rib wall facing the flow direction. The recirculation down stream of the rib can move some particles backwards; however, this phenomenon occurs at low y/h, therefore the particles have a higher probability to deposit on the bottom wall of the channel. This is confirmed by Figs. 15 and 16a and b. Fig. 15 shows a typical distribution of particles in the x–y plane (for fine LES and for a simulation time $60L_x/u_0$); Fig. 16a gives a detailed view near the rib and Fig. 16b a detailed view near the

smooth top channel surface wall. As expected, see for instance Chamberlain (1966, 1967, 1968), Lai et al. (1999, 2001) and Li and Ahmadi (1993), the simulation also exhibits a much higher deposition on the rough (ribbed) wall compared with the smooth wall.

As can be seen from Fig. 13, the coarse and fine grid particle predictions are fairly similar. However, stronger discrepancies between fine and coarse LES have been observed downstream the rib, where the coarse LES tends to predict a higher deposition. In spite of this, the at least qualitative level of agreement between fine and coarse LES results convinced us to carry out all other simulations with different particles and gravity directions mostly on the coarse grid. Simulations with $\mathbf{g} = -g\mathbf{i}$ and $\mathbf{g} = g\mathbf{j}$ (not shown) suggest that generally gravity direction has relatively little influence. As
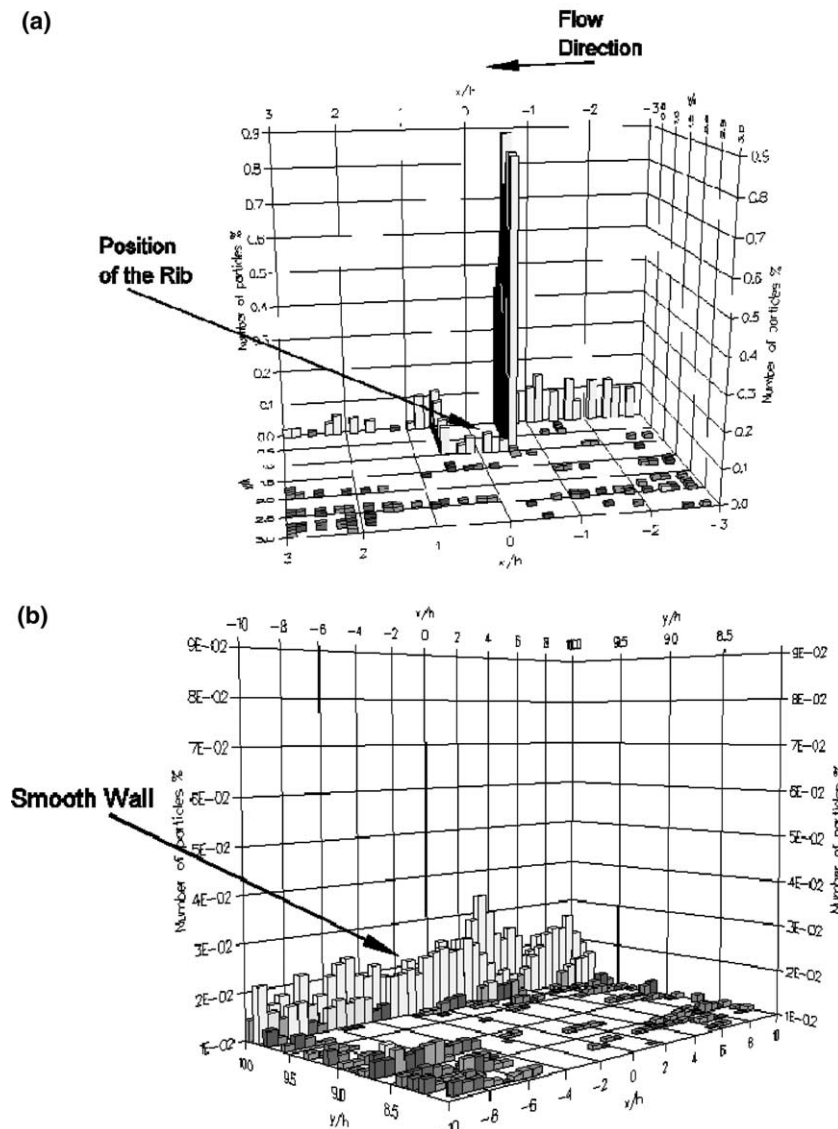

Fig. 16. Particle concentration: (a) detail near the rib and (b) detail near the smooth wall.

expected, when the $\mathbf{g} = -g\mathbf{i}$ (opposite to the flow direction) there is less deposition onto the left wall of the rib. A similar survey has been carried out for heavy particles ($d_p = 46.5\ \mu m$, $\rho_p = 8900\ kg/m^3$) with $\mathbf{g} = g\mathbf{k}$. Depositions are qualitatively the same as for the light particles and therefore not shown. It is important to note that there is less heavy particle deposition onto the rib walls (more precisely, after 200 wall time units, the concentration of heavy particles is almost an order of magnitude less than for light particles). Perhaps this is because low inertia particles are more easily entrained from the region above the rib toward the bottom while heavier particles just above the rib tend to move in straighter lines. Nonetheless even for heavy particles the ratios deposition fluxes onto the left and right facing ribs are similar. The motion of fibres/cylinders ($\rho_p = 8900\ kg/m^3$, diameter: $d_p = 87\ \mu m$, length: $l = 870\ \mu m$) with $\mathbf{g} = g\mathbf{k}$, is also investigated. In the simulations presented here, spherical particles and cylindrical particles have different particle relaxation times; therefore a consistent comparison of their deposition rate, i.e. the ratio of the flux of particles at the wall to the particle concentration, was not possible. The model has been verified by relating the model predictions to established empirical equations. This has been done in the following way. For a plane channel flow, Wood (1981) proposed an empirical model for the deposition rate V_d^+ of spherical particles as function of the particle relaxation time τ_p^+. Based on Wood's work and along the lines of Shapiro and Goldenberg (1993), Kvasnak and Ahmadi (1995) proposed an equivalent expression of the deposition velocity $\widetilde{V}_d^+$ for fibres. Model predictions for the number of spherical and cylindrical particles deposited onto the smooth wall of the ribbed channel (respectively N_{dep} and $\widetilde{N}_{dep}$) were compared with the empirical relation $\widetilde{V}_d^+(\tilde{\tau}_p)/V_d^+(\tau_p)$; here $\tilde{\tau}_p$ is an equivalent particle relaxation time for cylindrical particles, evaluated as (Shapiro and Goldenberg, 1993):

$$\tilde{\tau}_p^+ = \frac{2\beta S d_d^{+2}}{9} \frac{\ln\left(\beta + \sqrt{\beta^2 - 1}\right)}{\sqrt{\beta^2 - 1}} \tag{10}$$
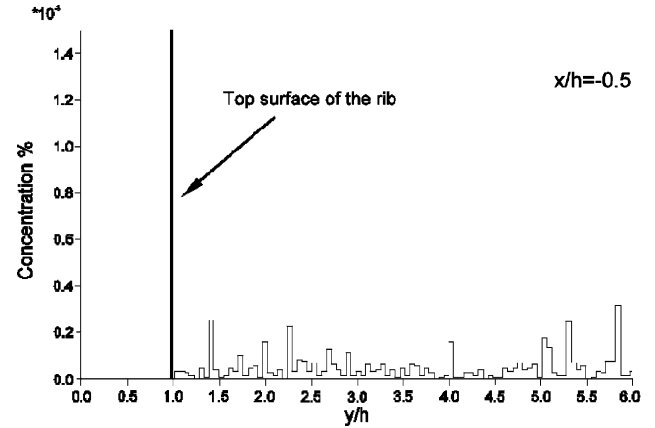

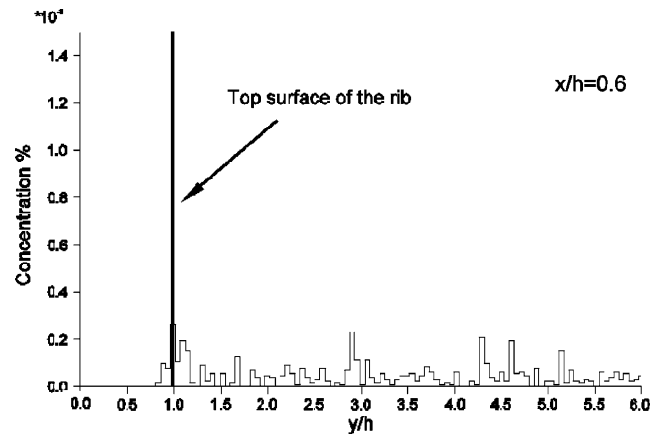Fig. 17. Cylindrical particle concentration at $x/h = -0.5$. Same configuration as shown in Fig. 13.

Fig. 18. Cylindrical particle concentration at $x/h = 0.6$. Same configuration as shown in Fig. 13.

where β is the length–diameter ratio and S is the particle–fluid density ratio. The results of the numerical simulation $\widetilde{N}_{dep}/N_{dep} = 11$ compare favourably with the prediction from established empirical relation $\widetilde{V}_d^+(\tilde{\tau}_p)/V_d^+(\tau_p) = 11.6$.

Figs. 17 and 18 give fibre concentrations. As can be seen (cf. Figs. 13 and 14), relative to spherical particles the concentration is highly attenuated in the rib
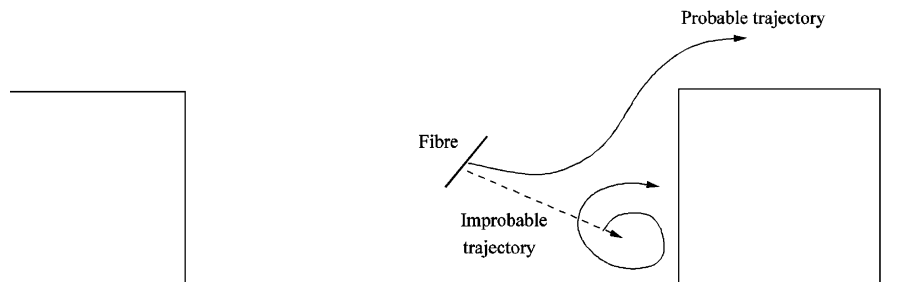

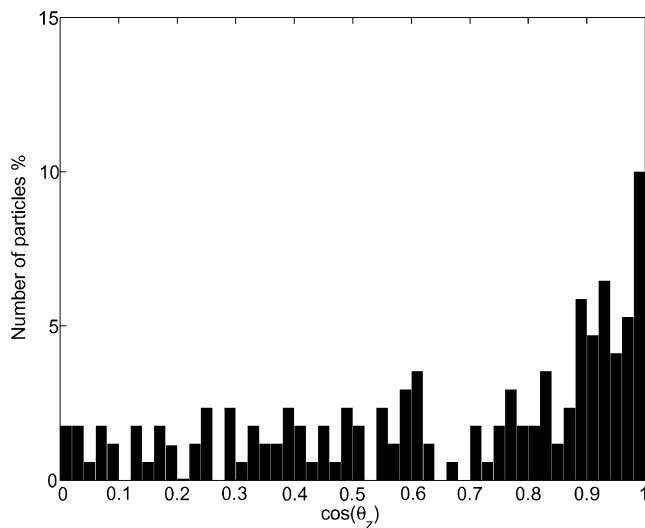Fig. 19. Schematic of the near rib fibre deposition.

Fig. 20. Angular distributions of fibres.

proximity, even on the left side (facing the flow direction). The results suggest fibres are unable to cross the corner recirculations, tending concentrate in low mean-flow vorticity regions (e.g. the central region of the channel). Fig. 19 gives an intuitive picture of this behaviour. In fact, according to the orientation of the fibres, particle trajectories that cross over mean-flow streamlines are less probable than those that follow them. Analysis of forces introduced in Section 2.2 clarifies this. The modelled forces generate a torque that aligns the cylinder with the local fluid velocity. Therefore in a shear flow it is expected that fibres, on average, tend to align with the direction of the mean flow. This is confirmed by Fig. 20, which shows the angular distribution of fibres. As can be seen, the higher concentration is when $|\cos(\theta) = 1|$.

5. Conclusions

The deposition characteristics of spherical and cylindrical particles in a periodic ribbed channel flow with $Re = 7000$ was examined in numerical simulations. Results suggested that spherical particles tend to accumulate on the rib wall facing the mean-flow direction. This preferential deposition did not arise for cylindrical particles. Consequently, cylindrical particles cannot be idealized as spherical particles with some effective aerodynamic response time and density.

Further simulations of cylindrical particles on a wider range of the density, diameter and length of the cylinder are worthy of investigation. As shown by Maxey (1990), different values of these parameters results in different transport characteristics.

The model for cylindrical particle movement is relatively easy to implement and can be readily extended to account for end-effects and fibre bending.

References

Acharya, S., Dutta, S., Myrum, T.A., Baker, R.S., 1993. Periodically developed flow and heat transfer in a ribbed duct. J. Heat Mass Transfer 36 (8), 2069–2982.

Armenio, V., Piomelli, U., Fiorotto, V., 1999a. Effect of the subgrid scales on particle motion. Phys. Fluids 11 (10), 3030–3042.

Armenio, V., Piomelli, U., Fiorotto, V., 1999b. On the application of large-eddy simulation to particle-laden flows. In: Banerjee, S., Eaton, J.K. (Eds.), 1st Int. Symp. on Turbulence and Shear Flow Phenomena—1, Santa Barbara, CA, pp. 139–144.

Brenner, H., 1964. The Stokes resistance of an arbitrary particle—IV, arbitrary fields of flow. Chem. Eng. Sci. 19, 703–727.

Chamberlain, A.C., 1966. Transport of gases to and from grass-like surfaces. Proc. Roy. Soc. A 290, 236–265.

Chamberlain, A.C., 1967. Transport of Lycopodium spores and other small particles to rough surfaces. Proc. Roy. Soc. A 296, 45–70.

Chamberlain, A.C., 1968. Transport of gases to and from surfaces with bluff and wave-like roughness elements. Quart. J. Roy. Meteorol. Soc. 94, 318–332.

Chamberlain, A.C., Garland, J.A., Wells, A.C., 1984. Transport of gases and particles to surfaces with widely spaced roughness element. Boundary-layer Meteorol. 29, 343–360.

Chung, Y.M., Tucker, P.G., 2003. Large-eddy simulation of an electronic system flow. In: Proc. 3rd Int. Symp. on Turbulence and Shear Flow Phenomena, Sendai, Japan, June 25–27, vol. II, pp. 675–680.

Clift, R., Grace, J.R., Weber, M.E., 1978. Bubbles, Drops and Particles. Academic Press, New York.

Deardoff, J.W., 1970. A numerical study of three-dimensional turbulent channel flow at large Reynolds number. J. Fluid Mech. 41, 453–480.

Fan, F.G., Ahmadi, G., 1990. Dispersion of non-spherical particles in a simulated isotropic turbulent field. Bull. Am. Phys. Soc. 35, 2271.

Fan, F.G., Ahmadi, G., 1995a. Dispersion of ellipsoidal particles in an isotropic pseudo-turbulent flow field. ASME J. Fluids Eng. 117, 154–161.

Fan, F.G., Ahmadi, G., 1995b. A sublayer model for wall deposition of ellipsoidal particles in turbulent streams. J. Aerosol Sci. 26 (5), 813–840.

Houghton, E.L., Carpenter, P.W., 1993. Aerodynamics for Engineering Students. Edward Arnold, London.

Jeffery, G.B., 1922. The motion of ellipsoidal particles immersed in a viscous fluid. Proc. Roy. Soc. A 102, 161–179.

Khayat, R.E., Cox, R.G., 1989. Inertia effect on the motion of long slender bodies. J. Fluid Mech. 209, 435–462.

Kvasnak, W., Ahmadi, G., 1995. Fibrous particle deposition in a turbulent channel flow: an experimental study. Aerosol Sci. Technol. 23, 641–652.

Lai, A.C.K., Byrne, M.A., Goddard, A.J.H., 1999. Measured deposition of aerosol particles on a two-dimensional ribbed surfaces in a turbulent duct flow. J. Aerosol Sci. 30, 1201–1214.

Lai, A.C.K., Byrne, M.A., Goddard, A.J.H., 2001. Aerosol deposition in turbulent channel flow on a regular array of three-dimensional roughness elements. J. Aerosol Sci. 32 (1), 121–137.

Li, A., Ahmadi, G., 1993. Computer simulation of deposition of aerosols in a turbulent channel flow with rough wall. Aerosol Sci. Technol. 18, 11–24.

Lo Iacono, G., Tucker, P.G., 2003. Numerical Study of Particle Motion in a Turbulent Ribbed Duct Flow. PhD thesis, University of Warwick, Coventry, United Kingdom.

Maxey, M.R., 1990. On the advection of spherical and non-spherical particles in a non-uniform flow. Philos. Trans. Roy. Soc. Lond. A 333, 289–307.

McLaughlin, J.B., 1989. Aerosol particle deposition in numerically simulated channel flow. Phys. Fluids 1 (7), 1211–1224.

Mei, R., 1992. An approximate expression for the shear lift force on a spherical particle at finite Reynolds number. Int. J. Multiphase Flow 18 (1), 145–147.

Meneveau, C., 1994. Statistics of turbulence subgrid-scale stresses: necessary conditions and experimental tests. Phys. Fluids 6 (2), 815–833.

Olson, J.A., Kerekes, R.J., 1998. The motion of fibres in turbulent flow. J. Fluid Mech. 377, 47–64.

Saffman, P.G., 1965. The lift on a small sphere in a slow shear flow. J. Fluid Mech. 22, 385–400, Corrigendum 31 (1968) 624.

Schlichting, H., Gersten, K., 2000. Boundary-layer Theory. Springer, London.

Shapiro, M., Goldenberg, M., 1993. Deposition of glass fiber particles from turbulent air flow in a pipe. J. Aerosol Sci. 24, 65–87.

Smagorinsky, J., 1963. General circulation experiment with the primitive equations, I. The basic experiment. Mon. Weather Rev. 91 (3), 99–164.

Tucker, P.G., 2001a. Computation of particle and scalar transport for complex geometry turbulent flows. ASME J. Fluids Eng. 123, 372–381.

Tucker, P.G., 2001b. Computation of Unsteady Internal Flows. Kluwer Academic, Norwell, MA.

Tucker, P.G., 2004. Hybrid MILES-RANS method for more dissipative solvers and the use of non-linear LES. In: 42nd Aerospace Sciences Meeting and Exhibit, Reno, Paper Number AIAA-2004-0071.

Tucker, P.G., Pan, Z., 2001. URANS computations for a complex internal isothermal flow. Comput. Methods Appl. Mech. Eng. 190, 2893–2907.

Wang, Q., Squires, K.D., 1996. Large eddy simulation of particle deposition in a vertical turbulent channel flow. Int. J. Multiphase Flow 22 (4), 667–683.

Wood, N.B., 1981. The mass transfer of particles and acid vapour to cooled surfaces. J. Inst. Energy 76, 76–93.

Yeh, F.G., Lei, U., 1991. On the motion of small particles in a homogeneous isotropic turbulent flow. Phys. Fluids A 3, 2571–2586.

Zhang, H., Ahmadi, G., Fan, F.G., McLaughlin, J.B., 2001. Ellipsoidal particles transport and deposition in turbulent channel flows. Int. J. Multiphase Flow 27 (27), 971–1009.